Journal of Zhejiang University-SCIENCE A (Applied Physics & Engineering)
ISSN 1673-565X (Print); ISSN 1862-1775 (Online)
www.zju.edu.cn/jzus; www.springerlink.com
E-mail: jzus@zju.edu.cn

Numerical study on performance of perforated plate applied to cryogenic fluid flowmeter*

Hai-fei LIU[1], Hong TIAN[2], Hong CHEN[1], Tao JIN[2], Ke TANG[†‡2]
(*[1]State Key Laboratory of Technologies in Space Cryogenic Propellants, Beijing 100028, China*)
(*[2]Institute of Refrigeration and Cryogenic, Key Laboratory of Refrigeration and Cryogenic Technology of Zhejiang Province,*
Zhejiang University, Hangzhou 310027, China)
[†]E-mail: ktang@zju.edu.cn

Received Apr. 7, 2015; Revision accepted June 25, 2015; Crosschecked Feb. 29, 2016

Abstract: The perforated plate is one of the effective devices for measuring flow rate accurately. In this study, a perforated plate is investigated for its characteristics, mainly including discharge coefficient C and pressure loss coefficient ζ, when applied to cryogenic fluids with the help of ANSYS Fluent. Three cryogenic fluids are studied, including liquid nitrogen (LN_2), liquid oxygen (LO_2), and liquid hydrogen (LH_2). For comparison, two states of water are also investigated. The realizable κ-ε model with standard wall function is used to describe the turbulence and simulate the near-wall flow. The Schnerr-Sauer cavitation model is used to investigate the effect of cavitation on the performance of the perforated plate. Simulation results indicate that the upper limit of Reynolds number of the perforated plate is significantly dependent on the properties of the measured fluid when the temperatures of the fluids are set as the normal boiling point temperatures and the outlet pressures are 0.2 MPa.

Key words: Perforated plate, Flowmeter, Cryogenic fluids, Discharge coefficient, Pressure loss coefficient
http://dx.doi.org/10.1631/jzus.A1500082 **CLC number:** TK313

1 Introduction

Differential pressure devices such as orifices, venturis, and nozzles are frequently used in flow rate measurement. Among these devices, the orifices have been standardized and widely used for their advantages, such as simplicity in design, installation, and replacement; relatively low cost; and the absence of moving parts. However, they also have the disadvantages of high permanent pressure loss, sensitivity to incoming flow distortions, and nonlinearity (Shaaban, 2014). Compared with the standard orifice, the perforated plate (with multiple holes distributed on it) can balance the flow, introduce less turbulence, and reduce energy loss. The applications of perforated plate have attracted considerable interest in the fields of chemical, pharmaceutical, and pulp and paper plants to measure the flow rate in their piping systems.

The reported work of the perforated plates mainly focused on two performance parameters, i.e., the discharge coefficient and the pressure loss coefficient. The discharge coefficient relates the actual flow rate to the theoretical flow rate (ISO, 2003a), and the pressure loss coefficient denotes the permanent pressure loss. Kolodzie and van Winkle (1957) experimentally studied the discharge coefficient of perforated plates with air and correlated the discharge coefficient with the geometric parameters, such as plate thickness and perforated area. Smith and van Winkle (1958) expanded the Reynolds number (Re) range in the correlation established by Kolodzie and van Winkle (1957) (from 400 to

---

[‡] Corresponding author

[*] Project supported by the State Key Laboratory of Technologies in Space Cryogenic Propellants (No. SKLTSCP1208), China

ORCID: Hai-fei LIU, http://orcid.org/0000-0002-6276-276X

20 000). Huang *et al.* (2013) studied the effects of the geometry and the upstream disturbance on the discharge coefficient of perforated plate using water and pointed out that a perforated plate had a lower critical Reynolds number and a stronger anti-disturbance ability compared with the standard orifice. As for the permanent pressure loss, Gan and Riffat (1997) determined the pressure loss coefficient of air passing perforated plates in a square pipe by means of numerical simulations and experimental tests. Erdal (1998) performed a numerical study of the parameters affecting the dissipation characteristics of the perforated plate. Testud *et al.* (2007) discussed the cavitation and the related pressure loss of water passing through perforated plates by experimental observation. Zhao *et al.* (2011) investigated the dissipation characteristics of several perforated plates with water and reported an empirical formula for estimating the pressure drop. Malavasi and Messa (2011) and Malavasi *et al.* (2012) numerically studied the dissipation and cavitation characteristics of perforated plates and, then, experimentally studied the dependence of the pressure loss coefficient on *Re*, the equivalent diameter ratio, etc., with water as operating fluid. Guo *et al.* (2013) numerically simulated the effect of geometry, wall roughness, and inclination angle on the pressure loss with dry air. Maynes *et al.* (2013) analyzed the pressure loss coefficient and the onset of cavitation caused by water flow through perforated plates and established two correlations relating the incipient and critical cavitation numbers to the geometrical parameters of perforated plates.

The above-mentioned work mainly investigated the performance of perforated plates with common fluids, such as water and air, around ambient temperature. However, little effort has been similarly made in the case of cryogenic fluids, which are widely used in the field of air separation industry, aerospace application, etc. The distinct properties of cryogenic fluids may induce varied performances of perforated plates, which is of great importance for the design of a flowmeter for cryogenic fluids.

In this study, we numerically assess the performance of a perforated plate applied to a flowmeter for cryogenic fluids. The flow situations of three typical cryogenic fluids, i.e., liquid nitrogen (LN_2), liquid oxygen (LO_2), and liquid hydrogen (LH_2), through a perforated plate are simulated. Two cases of water are also simulated for comparison. Our emphasis is on the discharge coefficient and the pressure loss coefficient. It can be found that cryogenic fluids have much larger applicable ranges of *Re* for flow rate measurement than water. An analysis of the possible reasons is also presented.

2 Working principle of a perforated plate flowmeter and its key performance parameters

For a flowmeter with perforated plate, the volumetric flow rate q_v can be calculated by measuring the differential pressure ΔP across the perforated plate as the flow passage is restricted, based on Bernoulli's principle (Landau and Lifshitz, 2008), which can be given as follows (Huang *et al.*, 2013):

$$q_\mathrm{v}=\frac{C\varepsilon A_0}{\sqrt{1-\beta^4}}\sqrt{\frac{2\Delta P}{\rho}}, \tag{1}$$

where C is the discharge coefficient, ε is the expansibility factor (being unity for an incompressible fluid), A_0 denotes the total open area of the perforated plate, ρ is the fluid density, and β represents the equivalent diameter ratio ($\beta=\sqrt{A_0/A_\mathrm{p}}$, where A_p is the pipe cross-sectional area). The differential pressure ΔP is the pressure difference between the pressure taps, one of which is on the upstream side of a primary device, while the other is on the downstream side (ISO, 2003a). In the numerical simulations, the upstream and downstream pressures are measured as the pipe wall pressures at both ends of the perforated plate.

The discharge coefficient C relates the actual flow rate to the theoretical expression deduced with Bernoulli's principle for the flow of an ideal fluid. As one of the important parameters characterizing the performance of the perforated plate flowmeter, the value of C depends mainly on the plate geometry and *Re* (Huang *et al.*, 2013). There exists a range of *Re*, where C is roughly constant. This range of *Re* usually determines the measuring range of the perforated plate flowmeter. If possible, a larger constant C

is expected to reduce the pressure loss of the perforated plate (Huang *et al.*, 2013).

It should be noted, from Eq. (1), that the discharge coefficient C can be written as

$$C=\frac{q_{\mathrm{v}}\sqrt{1-\beta^{4}}}{\varepsilon A_{0}\sqrt{2\Delta P/\rho}},\tag{2}$$

i.e., C can be calculated with the known values of q_{v}, A_0, β, ρ, and the measured differential pressure ΔP.

Another important performance parameter is the pressure loss coefficient ζ, representing the dissipation characteristics of the perforated plate flowmeter and defined as follows (ISO, 2003b):

$$\zeta=\frac{\Delta\varpi}{\rho u^{2}/2},\tag{3}$$

where $\Delta\varpi$ represents the permanent pressure loss of the perforated plate and is calculated as the difference between the average pressure measured on the wall at the 1D (D is the inner diameter of pipe) upstream side of the perforated plate and that measured at the 6D downstream side of the perforated plate in the simulation, and u is the fluid velocity in the pipe. The difference between ΔP and $\Delta\varpi$ is shown in Fig. 1.

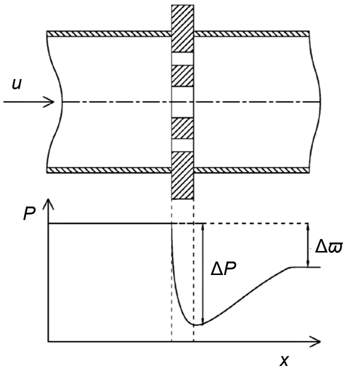

Fig. 1 Pressure distribution along the centerline of a perforated plate

3 Numerical model and validation

The geometry of the perforated plate studied in the present work is one of the examples experimentally investigated by Huang *et al.* (2013). The layout of the perforated plate is shown in Fig. 2. Fourteen holes are distributed over two homocentric circles, with five holes uniformly on the inner circle and nine holes uniformly on the outer circle.

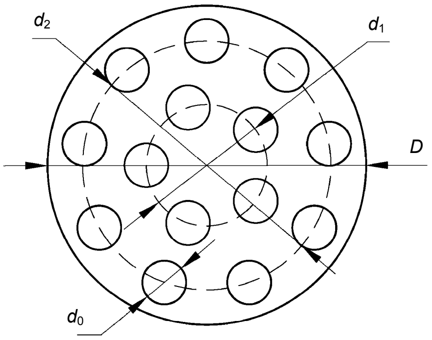

Fig. 2 Layout and dimensions of the holes on the perforated plate (Huang *et al.*, 2013)

All the holes have a same diameter d_0=4 mm. Five holes are located on the circle with a diameter d_1=11.02 mm; nine holes are located on the circle with a diameter d_2=22.62 mm. The inner diameter of the pipe is D=29 mm, thus, the equivalent diameter ratio is β=0.516. The thickness of the perforated plate is t=3 mm

3.1 Numerical model

Flow predictions are carried out in a horizontal pipe. The 1D schematic layout of the computational domain is shown in Fig. 3. Singh *et al.* (2006; 2009) found that the disturbance caused by various openings of the gate valve and imposed swirl has no significant effect on the discharge coefficient of the cone flowmeter when the disturbance is over 5D upstream from cone. Kumar and Bing (2011) used 5D upstream pipe length and 10D downstream pipe length to numerically study the slotted orifice meters. In this study, the length 10D upstream of the perforated plate is chosen to attain reliable prediction of the discharge coefficient and the pressure loss coefficient. A 15D downstream pipe length is provided to assure that the boundary condition at the exit does not affect the computational flow field close to the perforated plate. Hence, the entire flow profile can be acquired as the fluids come through the vena contracta.

The governing equations for cryogenic cavitation based on the mixture model include continuity, momentum, and energy equations; the κ-ε two

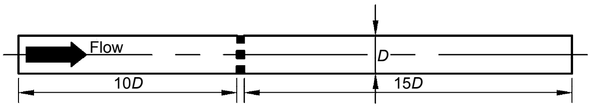

Fig. 3 1D schematic layout of the computational domain

equations; and a transport equation for the vapor volume fraction. The continuity, momentum, and energy equations for steady flow are as follows (Anderson, 1995; ANSYS Inc., 2012):

$$\nabla\cdot(\rho_{\mathrm{m}}\boldsymbol{u}_{\mathrm{m}})=0, \tag{4}$$

$$\nabla\cdot(\rho_{\mathrm{m}}\boldsymbol{u}_{\mathrm{m}}^{2})=-\nabla P +\nabla\cdot\left[(\mu_{\mathrm{m}}+\mu_{\mathrm{t}})\left(\nabla\boldsymbol{u}_{\mathrm{m}}+\nabla\boldsymbol{u}_{\mathrm{m}}^{\mathrm{T}}-\frac{2}{3}\nabla\boldsymbol{u}_{\mathrm{m}}\boldsymbol{I}\right)\right], \tag{5}$$

$$\rho_{\mathrm{m}}\boldsymbol{u}_{\mathrm{m}}\nabla T=\nabla\cdot[(\lambda_{\mathrm{m}}+\lambda_{\mathrm{t}})\nabla T]+S_{\mathrm{E}}, \tag{6}$$

where ρ_{m} is the mixture density, defined as $\rho_{\mathrm{m}}=\rho_{\mathrm{v}}\alpha+\rho_{\mathrm{l}}(1-\alpha)$ (ρ_{v} is the vapor phase density, α represents the vapor volume fraction, and ρ_{l} is the liquid phase density), $\boldsymbol{u}_{\mathrm{m}}$ is the velocity of the mixture, P is the pressure, $\boldsymbol{I}$ represents the unit tensor, T is the temperature, μ_{m} is the dynamic viscosity of the mixture, μ_{t} denotes the turbulent viscosity, λ_{m} is the mixture's thermal conductivity, λ_{t} is the turbulent thermal conductivity, and S_{E} is the volumetric heat source calculated with the phase-change mass and the latent heat. It is assumed that the flow is incompressible and there is no velocity slip between the liquid and vapor phases.

As for the turbulence model, both the realizable and the renormalization group (RNG) κ-ε models are considered. Both of the models have shown substantial improvements over the standard κ-ε model whereby the flow features include strong streamline curvature, vortices, and rotation. The comparison between the two turbulence models will be given in Section 3.2.

In the cavitation process, the liquid-vapor mass transfer (evaporation and condensation) is governed by the following vapor transport equation (ANSYS Inc., 2012):

$$\frac{\partial}{\partial t}(\alpha\rho_{\mathrm{v}})+\nabla\cdot(\alpha\rho_{\mathrm{v}}\boldsymbol{u}_{\mathrm{v}})=R, \tag{7}$$

where $\boldsymbol{u}_{\mathrm{v}}$ is the vapor phase velocity, and R represents the net mass transfer source term. Schnerr and Sauer (2001) adopted the Rayleigh-Plesset equation for bubble dynamics to deduce an expression for the net mass transfer source term R in the following forms:

$$R=\begin{cases} R_{\mathrm{g}}-R_{\mathrm{c}}=\dfrac{3\rho_{\mathrm{v}}\rho_{\mathrm{l}}}{\rho_{\mathrm{m}}}\alpha(1-\alpha)\left(\dfrac{\alpha}{1-\alpha}\dfrac{3}{4\pi}\dfrac{1}{n}\right)^{-\frac{1}{3}}\sqrt{\dfrac{2}{3}\dfrac{P_{\mathrm{v}}-P}{\rho_{\mathrm{l}}}}, \\ \qquad P\le P_{\mathrm{v}}, \\ R_{\mathrm{c}}-R_{\mathrm{g}}=\dfrac{3\rho_{\mathrm{v}}\rho_{\mathrm{l}}}{\rho_{\mathrm{m}}}\alpha(1-\alpha)\left(\dfrac{\alpha}{1-\alpha}\dfrac{3}{4\pi}\dfrac{1}{n}\right)^{-\frac{1}{3}}\sqrt{\dfrac{2}{3}\dfrac{P-P_{\mathrm{v}}}{\rho_{\mathrm{l}}}}, \\ \qquad P>P_{\mathrm{v}}, \end{cases} \tag{8}$$

where R_{g} and R_{c} are the mass transfer source terms related to the growth and collapse of vapor bubbles, respectively, P_{v} is the saturated vapor pressure, and n is the bubble number density, which is considered a constant. The two-phase equations will reduce to the single-phase one when no cavitation occurs.

In the simulation, the inlet and outlet of the pipe are set as uniform velocity and pressure boundary conditions, respectively. The inlet turbulence intensity I=0.16$Re^{-1/8}$ is determined under turbulence quantities varying with the inlet velocity. The hydraulic diameter maintains a constant value of 29 mm, which is equal to the pipe diameter in all the simulations. The pipe and the surface of the perforated plate are both specified as the wall with no-slip and heat insulation. The wall function and the inlet boundary condition for the temperature used in the simulation are specified later in this paper.

3.2 Model validation

The 3D geometry of the computational domain is created by using the GAMBIT preprocessor (Fluent Inc., USA). The flow domain is meshed with both structured and unstructured meshes. For efficient discretization, the whole geometry is divided into five regions: upstream, downstream, and central regions, and two joint regions connecting the central region to the upstream and downstream regions, respectively. Upstream and downstream regions with smooth flow condition are meshed with coarse hexagonal grids. The central perforated plate region is meshed with fine hexagonal meshes to capture the high velocity and pressure gradients. The two joint regions are meshed with unstructured tetrahedral hybrid cells from the point of transition effect. The meshed perforated plate and the magnification of one hole are shown in Fig. 4.

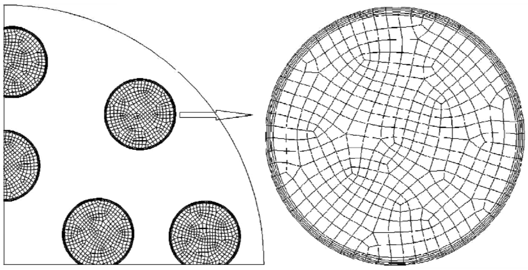

Fig. 4 Mesh for simulation of the perforated plate

Mesh size independency test is conducted to ensure that the numerical results are independent of mesh size and quality. Three numbers of cells, i.e., 796 936, 1 054 648, and 1 348 213, are used to carry out the test. In this section, LN_2 is selected as the working fluid, with the computational fluid dynamics (CFD) calculation being performed at the inlet velocity of 0.1 m/s, 2.0 m/s, 3.0 m/s, and 4.0 m/s. The discharge coefficient C is calculated using Eq. (2), with the differential pressure measured as the wall average pressure at the surfaces of the perforated plate. The results are shown in Fig. 5. The grid convergence index (GCI) (Roache, 1994) of LN_2 at the velocity of 3.0 m/s (Table 1) can be used to evaluate the grid independency. Considering the grid independency and the computation efficiency, the mesh with 1 054 648 cells is adopted in the following simulation.

The realizable κ-ε turbulence model (RKE) and the RNG κ-ε turbulence model (RNGKE) with standard wall functions (SWFs) and enhanced wall treatment (EWT) are considered in the simulation. Fig. 6 shows the comparison of the simulated discharge coefficient C, with the corresponding experimental values with water as working fluid under atmospheric pressure and room temperature (Huang *et al.*, 2013). It is found that all the values from the simulation are slightly smaller than the experimental values, and the RKE model with SWF (RKE-SWF) gives the best agreement with the experimental results, with deviations <5.5%, and is used in the following simulation.

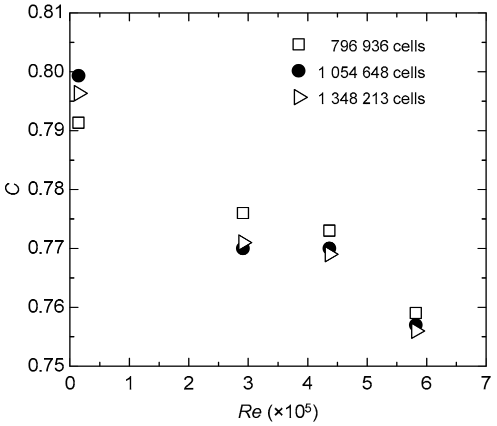

Fig. 5 Mesh size independency test

Table 1 Grid convergence index (GCI) of LN_2 at the velocity of 3.0 m/s

Number of cells	GCI (%)
From 1 358 213 to 1 054 648	0.196
From 1 054 648 to 796 936	0.578

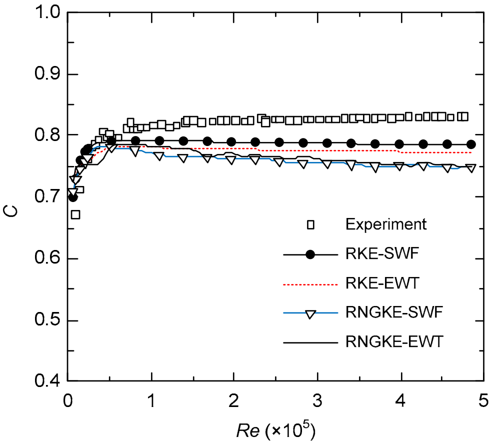

Fig. 6 Comparison between numerical and experimental results of discharge coefficient C

RKE-SWF: realizable κ-ε turbulence model with standard wall functions; RKE-EWT: realizable κ-ε turbulence model with enhanced wall treatment; RNGKE-SWF: renormalization group (RNG) κ-ε turbulence model with standard wall functions; RNGKE-EWT: RNG κ-ε turbulence model with enhanced wall treatment

To validate the Schnerr-Sauer cavitation model, a simulation was conducted and compared with experimental data in Hord (1973) for the case of the hydrofoil 283C, for which the boundary conditions are listed in Table 2. The experiment was conducted in a tunnel with a hydrofoil installed in it (Fig. 7, the

2D computational domain). In the simulation, a uniform velocity is specified at the inlet, and a pressure is set at the outlet. The cavitation number plays a role in implying the flow condition (Hord, 1973). Both the RKE model and the Schnerr-Sauer cavitation model are activated. As shown in Fig. 8, compared with the experimental data, the numerical values are acceptable in most cavitation regions, considering the instrumentation uncertainty of 6900 Pa for pressure and 0.2 K for temperature. Zhu *et al.* (2015) also proved that the Schnerr-Sauer cavitation model has a good performance in simulating cryogenic cavitation. Thus, the Schnerr-Sauer cavitation model is adopted in our simulations.

4 Results and discussion

After validation, the simulation mainly focuses on three cryogenic fluids and water at two states, i.e., liquid nitrogen (LN_2), liquid oxygen (LO_2), liquid hydrogen (LH_2), and water at two specific temperatures (denoted as Water1 and Water2, respectively). Table 3 lists the inlet free-stream temperature, outlet pressure, saturated vapor pressure, density, and kinematic viscosity of saturated liquid corresponding to the inlet free-stream temperature for the five fluids for the simulation. For LN_2, LO_2, LH_2, and Water1, the inlet free-stream temperatures are set as their normal boiling point temperatures, while ambient temperature is considered for Water2.

Table 2 Boundary conditions for the hydrofoil 283C (Hord, 1973)

Liquid	Free-stream temperature, T (K)	Free-stream velocity, u (m/s)	Cavitation number, K_v
LN_2	77.71	14.5	1.8

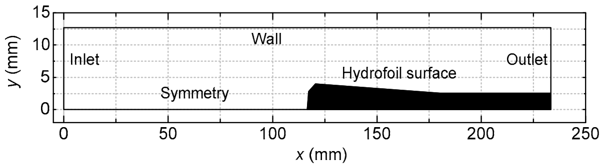

Fig. 7 Computational domain of the hydrofoil 283C for validating the Schnerr-Sauer cavitation model. The *x*- and *y*-axis scales are not equal for a better visualization

4.1 Typical simulated results of pressure, temperature, and vapor volume fraction

Taking LN_2 as an example, the typical simulated results of pressure and temperature 2*D* upstream and downstream from the perforated plate are shown in Fig. 9. The reference point (i.e., the origin of the horizontal axis) is located at the front surface of the perforated plate. The pressure has a dramatic drop at

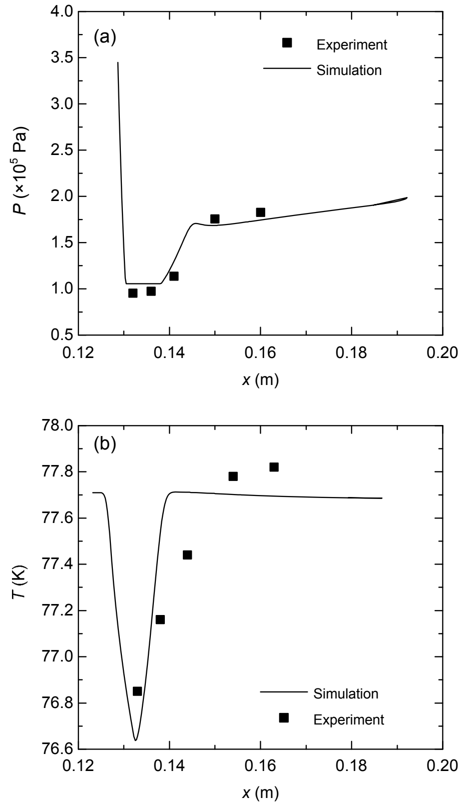

Fig. 8 Distributions of pressure (a) and temperature (b) along the hydrofoil wall from computation

Table 3 Conditions and corresponding properties of the fluids

Liquid	Inlet free-stream temperature, T (K)	Outlet pressure, P (MPa)	Saturated vapor pressure, P_v (Pa)	Liquid density, ρ (kg/m^3)	Liquid kinematic viscosity, v (cm^2/s)	ρv^2 ($\times10^{-6}$ kg·cm/s^2)
LN_2	77.36	0.2	101 385	806.08	0.001 993	0.003 20
LO_2	90.19	0.2	101 348	1142.00	0.001 706	0.003 32
LH_2	20.37	0.2	101 358	70.85	0.001 880	0.000 25
Water1	373.15	0.2	101 418	958.38	0.002 938	0.008 27
Water2	293.15	0.2	2339	998.20	0.010 040	0.100 62

the front surface of the perforated plate, followed by a gradual increase till the distance of roughly 1*D* downstream (Fig. 9a). This can be attributed to the variation of velocity according to Bernoulli's principle (Landau and Lifshitz, 2008).

Additionally, cavitation occurs when the pressure drops below the local saturated vapor pressure, and the temperature at the low-pressure zone will drop due to the heat effect of evaporation. For the case of 4.0 m/s, there is a visible temperature drop (Fig. 9b), which can also be found in the contour of vapor volume fraction near the perforated plate, as presented in Fig. 10.

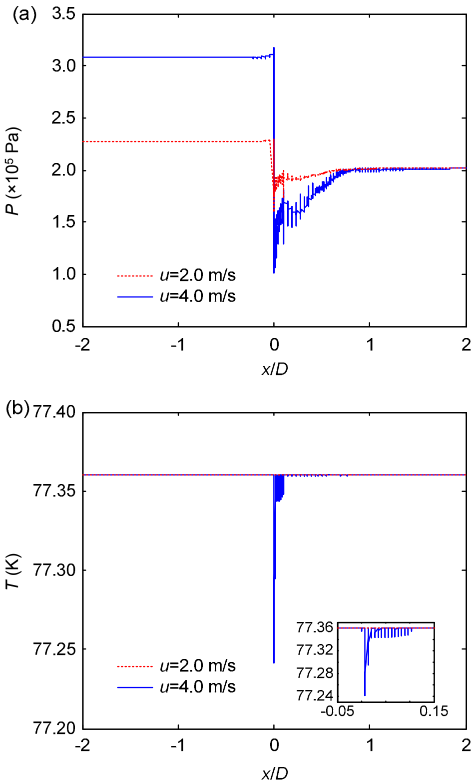

Fig. 9 Pressure (a) and temperature (b) profiles upstream/downstream of the perforated plate along the pipe. The inset in (b) shows the detailed *T* around *x*=0

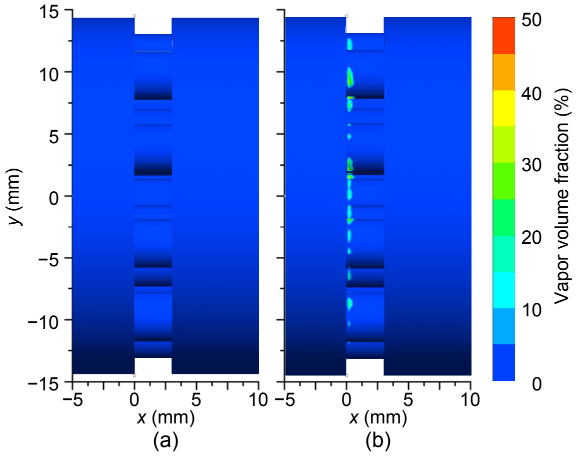

Fig. 10 Contour of vapor volume fraction of LN_2: (a) *u*=2.0 m/s; (b) *u*=4.0 m/s. References to color refer to the online version of this paper

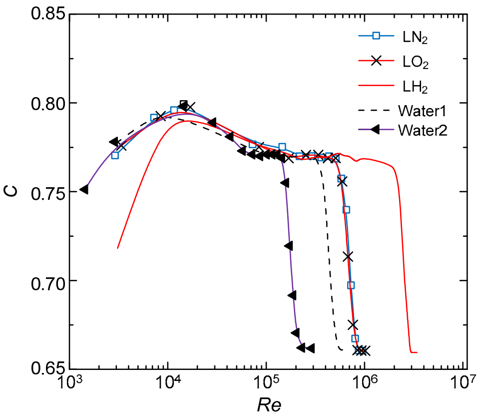

Fig. 11 Variation of discharge coefficient with Reynolds number

4.2 Discharge coefficient

The variation of discharge coefficient *C* with Reynolds number *Re* is shown in Fig. 11. Three different regions (i.e., unstable, stable, and cavitation region) can be identified for each fluid. In the unstable region with relatively small *Re*, the unstable flow leads to variable discharge coefficient as a function of *Re* (Huang *et al*., 2013). For the stable region, the volumetric flow rate q_v is proportional to the square root of the differential pressure ΔP, with almost constant discharge coefficient, which is preferred for the flow rate measurement application. However, a further increase in *Re* will lead to an abrupt drop in discharge coefficient, which indicates the appearance of cavitation. The occurrence of liquid/vapor two-phase flow in cavitation can result in an abrupt rise in pressure drop, which then leads to the abrupt decrease in the discharge. Thus, besides the disadvantages of the cavitation erosion and the increased pressure loss, from the viewpoint of the varying discharge coefficient, the cavitation region should be avoided for the flowmeter application.

As mentioned above, the flow rate measurement with a perforated plate focuses on the stable region of the discharge coefficient. The approximate ranges of *Re* for the stable region of the five fluids obtained from Fig. 11 are listed in Table 4 with the corresponding average discharge coefficient $\bar{C}$ and the standard deviations σ.

It can be seen that $\bar{C}$ is almost the same for all the five fluids in the stable region, which is not surprising but a direct result of the CFD model, whereas the ranges of *Re* are different. The lower limits of the *Re* for the constant discharge coefficient, the so-called critical Reynolds number Re_c (Huang *et al.*, 2013), are relatively close, i.e., in the range of 5.77×10^4 to 9.87×10^4. It means that the Re_c is probably determined mainly by the geometry of the perforated plate. However, for the upper limits of Reynolds number (denoted as Re_{up}), there are quite large differences for diverse fluids, with a maximum of 216.00×10^4 for LH_2 and a minimum of 15.90×10^4 for Water2. In addition, the values of standard deviation indicate that the discharge coefficient has a good stability in the stable region for the five fluids.

Table 4 Ranges of *Re* for the stable region and the corresponding values of average discharge coefficient $\bar{C}$ and standard deviation σ for the five fluids

Fluid	Range of *Re* ($\times10^4$)	$\bar{C}$	σ ($\times10^{-4}$)
LN_2	7.27–58.20	0.770	5.89
LO_2	8.45–59.20	0.768	5.96
LH_2	7.71–216.00	0.768	4.47
Water1	9.87–39.50	0.768	5.64
Water2	5.77–15.90	0.769	7.77

We attempt to give some explanations for the relatively large different Re_{up} values from the properties of the fluids. The pressure drop of the fluid through the perforated plate can be calculated by (Idelchik, 1989)

$$\Delta P = \xi \rho \frac{u^2}{2}, \tag{9}$$

where ξ is the resistance coefficient, depending on the geometry of the perforated plate. Eq. (9) can be rewritten as

$$\Delta P = \frac{\xi Re^2}{2D^2} \rho v^2. \tag{10}$$

According to Eq. (10), for a given *Re*, the pressure drop caused by the perforated plate is proportional to the product of the density and the squared kinematic viscosity, i.e., ρv^2. Table 3 shows that, compared with water, the cryogenic liquids (LN_2, LO_2, and LH_2, especially LH_2) have smaller values of ρv^2. Therefore, with a fixed *Re*, the pressure drops through the perforated plate for these cryogenic fluids are much less than that for water. In addition, the saturated vapor pressures P_v of the three cryogenic fluids and Water1 in this study are almost equal to the atmospheric pressures because the temperatures of the fluids are set at the normal boiling point temperatures. Thus, the occurrence of cavitation is more difficult for the three cryogenic fluids under comparable thermofluid dynamic conditions, i.e., the same pressure at the outlet section. As for Water2 at ambient temperature, its saturated vapor pressure is lower than those of the three cryogenic fluids at their normal boiling temperatures; however, the much larger pressure drop due to the much larger ρv^2 of Water2 leads to the occurrence of cavitation at relatively low *Re*, i.e., low Re_{up}, in comparison with the three cryogenic fluids.

4.3 Pressure loss coefficient

Similar to the discharge coefficient as shown in Fig. 11, the pressure loss coefficient ζ has different dependence on *Re* for the unstable, stable, and cavitation regions (Fig. 12). In the stable region, the pressure loss coefficient is not only roughly a constant, independent of *Re*, but also smaller than those in the other two regions. The liquid/vapor two-phase

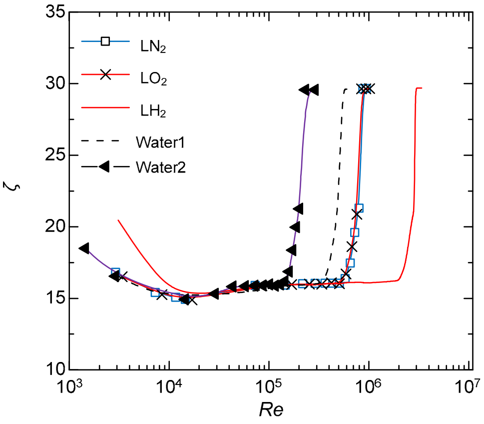

Fig. 12 Variation of pressure loss coefficient with Reynolds number

flow caused by the occurrence of cavitation increases the flow resistance, resulting in a marked rise in the pressure loss coefficient. A lower permanent pressure loss, indicated by the smaller pressure loss coefficient, is beneficial for the flowmeter application. Meanwhile, the constant pressure loss coefficient is almost not affected by the type of fluid, which is not surprising, being a direct consequence of the CFD model. However, for the investigated cryogenic fluids, especially LH_2, the pressure loss coefficient can remain constant even in the case of much larger Re. This can be attributed to the larger Re_{up} related to the occurrence of cavitation, as mentioned in Section 4.2.

5 Conclusions

Numerical simulations have been carried out to investigate the characteristics of a perforated plate with five working fluids, including three cryogenic fluids (LN_2, LO_2, and LH_2) at normal boiling point temperature and two different states of water (Water1 at normal boiling point temperature and Water2 at ambient temperature). The discharge coefficient and the pressure loss coefficient with the same pressure at the outlet section are focused on, with the following conclusions:

1. Compared with water, the cryogenic fluids have wider stable Reynolds number ranges, which are beneficial for the flow rate measurement. The lower limits of the Reynolds number of the stable region, which may be determined mainly by the geometry of the perforated plate, are relatively close for the five fluids investigated, i.e., in the range of 5.77×10^4 to 9.87×10^4. However, the upper limits of the Reynolds number related to the cavitation are much higher for the cryogenic fluids. From the viewpoint of flow rate measurement, the cavitation region should be avoided due to the decrease in the discharge coefficient and the increase in the pressure loss coefficient caused by the cavitation.

2. In the simulation, the saturated vapor pressures P_{v} of diverse fluids are all almost equal to the atmosphere pressures because the temperatures of the fluids are set at the normal boiling point temperatures. Consequently, the occurrence of cavitation is directly related to the pressure drop at the perforated plates, which is determined by the product of the density and the squared kinematic viscosity, i.e., ρv^2, of the working fluid for a given perforated plate geometry and a fixed Reynolds number. The much higher upper limits of Reynolds number for the cryogenic fluids can be attributed to the smaller ρv^2 compared with water.

References

Anderson, J.D., 1995. Computational Fluid Dynamics—the Basics with Applications. McGraw-Hill Inc., New York.

ANSYS Inc., 2012. Theory Guide, ANSYS FLUENT 14.5 Documentation. ANSYS Inc.

Erdal, A., 1998. A numerical investigation of different parameters that affect the performance of a flow conditioner. *Flow Measurement and Instrumentation*, **8**(2):93-102. http://dx.doi.org/10.1016/S0955-5986(97)00032-0

Gan, G.H., Riffat, S.B., 1997. Pressure loss characteristics of orifice and perforated plates. *Experimental Thermal and Fluid Science*, **14**(2):160-165. http://dx.doi.org/10.1016/S0894-1777(96)00041-6

Guo, B.Y., Hou, Q.F., Yu, A.B., *et al.*, 2013. Numerical modelling of the gas flow through perforated plates. *Chemical Engineering Research and Design*, **91**(3):403-408. http://dx.doi.org/10.1016/j.cherd.2012.10.004

Hord, J., 1973. Cavitation in Liquid Cryogens. 2: Hydrofoil. Technical Report No. NASA-CR-2156, National Aeronautics and Space Administrator. Available from http://ntrs.nasa.gov/search.jsp?R=19730007528 [Accessed on Jan. 15, 2014]

Huang, S.F., Ma, T.Y., Wang, D., *et al.*, 2013. Study on discharge coefficient of perforated orifices as a new kind of flowmeter. *Experimental Thermal and Fluid Science*, **46**:74-83. http://dx.doi.org/10.1016/j.expthermflusci.2012.11.022

Idelchik, I.E., 1989. Flow Resistance: a Design Guide for Engineers. Hemisphere Publishing Corporation, New York, p.69-75.

ISO (International Organization for Standardization), 2003a. Measurement of Fluid Flow by Means of Pressure Differential Devices Inserted in Circular Cross-section Conduits Running Full—Part 1: General Principles and Requirements, ISO 5167-1:2003. ISO, Geneva.

ISO (International Organization for Standardization), 2003b. Measurement of Fluid Flow by Means of Pressure Differential Devices Inserted in Circular Cross-section Conduits Running Full—Part 2: Orifice Plates, ISO 5167-2:2003. ISO, Geneva.

Kolodzie, P.A.Jr., van Winkle, M., 1957. Discharge coefficients through perforated plates. *AIChE Journal*, **3**(3):305-312. http://dx.doi.org/10.1002/aic.690030304

Kumar, P., Bing, M.W.M., 2011. A CFD study of low pressure wet gas metering using slotted orifice meters. *Flow Measurement and Instrumentation*, **22**(1):33-42.

http://dx.doi.org/10.1016/j.flowmeasinst.2010.12.002

Landau, L.D., Lifshitz, E.M., 2008. Fluid Mechanics: Volume 6 (Course of Theoretical Physics). Beijing Word Publishing Corporation, Beijing, China, p.8-9.

Malavasi, S., Messa, G., 2011. Dissipation and cavitation characteristics of single-hole orifices. *Journal of Fluids Engineering*, **133**(5):051302. http://dx.doi.org/10.1115/1.4004038

Malavasi, S., Messa, G., Fratino, U., *et al.*, 2012. On the pressure losses through perforated plates. *Flow Measurement and Instrumentation*, **28**:57-66. http://dx.doi.org/10.1016/j.flowmeasinst.2012.07.006

Maynes, D., Holt, G.J., Blotter, J., 2013. Cavitation inception and head loss due to liquid flow through perforated plates of varying thickness. *Journal of Fluids Engineering*, **135**(3):031302. http://dx.doi.org/10.1115/1.4023407

Roache, P.J., 1994. Perspective: a method for uniform reporting of grid refinement studies. *Journal of Fluids Engineering*, **116**(3):405-413. http://dx.doi.org/10.1115/1.2910291

Schnerr, G.H., Sauer, J., 2001. Physical and numerical modeling of unsteady cavitation dynamics. Proceedings of the 4th International Conference on Multiphase Flow, New Orleans, USA.

Shaaban, S., 2014. Optimization of orifice meter's energy consumption. *Chemical Engineering Research and Design*, **92**(6):1005-1015. http://dx.doi.org/10.1016/j.cherd.2013.08.022

Singh, R.K., Singh, S.N., Seshadri, V., 2009. Study on the effect of vertex angle and upstream swirl on the performance characteristics of cone flowmeter using CFD. *Flow Measurement and Instrumentation*, **20**(2):69-74. http://dx.doi.org/10.1016/j.flowmeasinst.2008.12.003

Singh, S.N., Seshadri, V., Singh, R.K., *et al.*, 2006. Effect of upstream flow disturbances on the performance characteristics of a V-cone flowmeter. *Flow Measurement and Instrumentation*, **17**(5):291-297. http://dx.doi.org/10.1016/j.flowmeasinst.2006.08.003

Smith, P.L.Jr., van Winkle, M., 1958. Discharge coefficients through perforated plates at Reynolds numbers of 400 to 3,000. *AIChE Journal*, **4**(3):266-268. http://dx.doi.org/10.1002/aic.690040306

Testud, P., Moussou, P., Hirschberg, A., *et al.*, 2007. Noise generated by cavitating single-hole and multi-hole orifices in a water pipe. *Journal of Fluids and Structures*, **23**(2):163-189. http://dx.doi.org/10.1016/j.jfluidstructs.2006.08.010

Zhao, T.Y., Zhang, J.L., Ma, L.D., 2011. A general structural design methodology for multi-hole orifices and its experimental application. *Journal of Mechanical Science and Technology*, **25**(9):2237-2246. http://dx.doi.org/10.1007/s12206-011-0706-3

Zhu, J.K., Chen, Y., Zhao, D.F., *et al.*, 2015. Extension of the Schnerr-Sauer model for cryogenic cavitation. *European Journal of Mechanics-B/Fluids*, **52**:1-10. http://dx.doi.org/10.1016/j.euromechflu.2015.01.008

中文概要

题　目： 应用于低温流体流量计的多孔板性能数值研究

目　的： 相较于常温流体，低温流体的物性存在显著不同，因而对流量计的工作特性也会带来相应的影响。本文旨在探讨多孔板应用于低温流体流量测量时的性能（即流出系数与压力损失系数）特征。

创新点： 基于数值研究结果，发现多孔板流量计应用于低温流体流量测量时，其稳定测量区间上限雷诺数显著增大，并基于物性特点从空化特性的角度探讨上限雷诺数显著增大的原因。

方　法： 采用数值模拟的方法，经网格独立性验证（表 1 和图 5）和模型验证（图 6 和图 8）后，结合 Realizable κ-ε 湍流模型与 Schnerr–Sauer 空化模型，研究同一种结构的多孔板应用于液氮、液氧、液氢三种低温流体和水流量测量时其流出系数与压力损失系数变化的异同（图 11、图 12 和表 5）；并基于低温流体的物性特点（表 3），对其具有较大上限雷诺数的计算结果进行原因分析。

结　论： 对于同一种多孔板结构，与水相比，低温流体具有较宽的稳定雷诺数测量范围，其中，与多孔板结构相关的下限雷诺数差异较小，而受空化影响的上限雷诺数差别较大；低温流体具有较大的上限雷诺数，其原因在于，与水相比较，低温流体的密度与运动粘度平方的乘积ρv^2明显较小。

关键词： 多孔板；流量计；低温流体；流出系数；压力损失系数